Resolving the debated atomic structure of the metastable cubic SiN_x tissue phase in nanocomposites with TiN

A. Fallqvist,[1] W. Olovsson,[1] B. Alling,[1,2] J. Palisaitis,[1] M. P. Belov,[3] I. A. Abrikosov,[1] L. Hultman,[1] and P. O. Å. Persson[1]

[1]*Department of Physics, Chemistry and Biology, Linköping University, SE-58183 Linköping, Sweden*

[2]*Max-Planck-Institut für Eisenforschung GmbH, D-402 37 Düsseldorf, Germany*

[3]*Materials Modeling and Development Laboratory, National University of Science and Technology MISIS, Leninskii pr 4, Moscow 119049, Russia*

(Received 24 January 2017; revised manuscript received 18 April 2017; published 20 September 2018)

The TiN/SiN_x nanocomposite and nanolaminate systems are the archetype for super if not ultrahard materials. Yet, the nature of the SiN_x tissue phase is debated. Here, we show by atomically resolved electron microscopy methods that SiN_x is epitaxially stabilized in a NaCl structure on the adjacent TiN(001) surfaces. Additionally, electron energy loss spectroscopy, supported by first-principles density functional theory calculations infer that SiN_x hosts Si vacancies.

DOI: 10.1103/PhysRevMaterials.2.093608

I. INTRODUCTION

Silicon nitride exists in several polytypes, where the most commonly known ones are the hexagonal β-Si_3N_4, α-Si_3N_4, and spinel-type γ-Si_3N_4. When silicon nitride is interfaced to other materials, a variety of structures are formed. A technologically relevant example is in nanocomposites, based on crystalline transition metal nitride nanoparticles percolated by a silicon nitride (SiN_x) matrix (tissue phase). These materials belong to the hardest known, and are therefore important for hard and superhard applications, e.g., in cutting tools. The hardness increase is generally attributed to the reduced dimensions, which prevent nucleation and motion of dislocations [1,2]. Additionally, the nanocomposite matrix provides strong intergranular bonds [3], while for other systems grain boundary sliding has proven detrimental [4]. The peak hardness for nanocomposites is found when the crystalline particles are in the range of 4–5 nm and embedded in a 1–2 monolayer thin tissue phase. Among the available nanocomposite systems, TiN-SiN_x has emerged as a prototype for understanding the physical properties. The TiN-SiN_x system is particularly interesting, because SiN_x has essentially no solubility in TiN. Hence, this nanocomposite is a consequence of a thermodynamically driven segregation of elements, resulting in chemically sharp interfaces between the crystalline particles and the tissue phase [5]. While the structure of the crystallites is normally well known for this family of nanocomposites, e.g., NaCl (B1) TiN in the TiN-SiN_x system, the structure of the interface and the SiN_x tissue phase is unknown. Initially the tissue phase was considered to be amorphous, while later on revised to "x-ray amorphous" [6]. The spatially limited dimensions and the random orientation of the nanoparticles makes it challenging to resolve this structure, even with the most powerful electron microscope.

In order to facilitate the investigations of the TiN/SiN_x interface, thin film model systems and multilayers/superlattices are used. This interface was initially investigated from crystalline TiN-Si_3N_4, where it was found that the hexagonal Si_3N_4 was aligned such that Si_3N_4[0001] ∥ TiN[110] and with Si_3N_4[10-10] ∥ TiN[111] [7]. Partially to limit the complexity, but also to investigate hardening mechanisms due to differences in shear modulus [8] and coherency strains [9], a number of experimental reports in recent years have successfully constructed multilayers and superlattices of TiN/SiN_x(001) [10–13]. Typically, 5-6 monolayers of epitaxial cubic SiN_x can be stabilized between TiN layers. With increasing SiN_x layer thickness, the entire layer assumes an amorphous structure and the epitaxial nature of the multilayers is lost. Since the epitaxial TiN/SiN_x interface is regarded as a key towards understanding the mechanisms for superhardening, the TiN/SiN_x interface has been subject to intense studies by complementary theoretical methods during the past decade [5,14–22]. Throughout these investigations both coherent and incoherent interfaces were investigated. However, the majority of the investigations involve NaCl (B1) or zincblende (B3) structures on either the (100) or (111) surfaces. Hao *et al.* [16–18] showed that depending on ambient nitrogen conditions, N-rich or N-poor, the SiN_x structure could assume preferentially octahedral Ti-Si-Ti bonds or tetrahedrally coordinated N-Si-N bonds, respectively, when sandwiched between TiN(111). Zhang [14,15] showed that it was possible to stabilize a monolayer of the B1 structure between adjacent TiN(111) or TiN(110) slabs. However, stabilization of SiN_x on the TiN(001) surface required a distortion of the Si-N bonds in the ⟨110⟩ direction to stabilize the structure. Following this work, Alling [19] showed that the both B1- and B3-SiN are dynamically unstable in bulk with respect to lattice vibrations, though by the introduction of Si vacancies, the B3 structure could be stabilized. By distorting the structure in the plane of the interface for the B1 configuration, Marten [20,21] showed that the stability of the structure was improved by the distortion of bonds at the (001) interface in agreement with Zhang; however, weak imaginary frequencies remained in the phonon spectrum indicating a slightly unstable configuration.

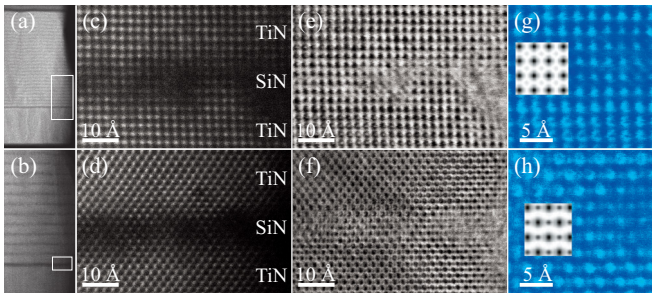

FIG. 1. Cross-sectional electron microscopy images of the TiN/SiN_x multilayer sample. The images in (a) and (b) show with different magnifications the multilayer structure used for the investigation. The inserted boxes identify the approximate region for image (b) and for the initial layer shown in (c)–(h). The images (c) and (d) show the high resolution HAADF-STEM images, across the first SiN_x layer as observed from ⟨100⟩and⟨110⟩, respectively. Images (e) and (f) show the simultaneously acquired ABF-STEM images. The false colored images in (g) and (h) show magnified views from (e) and (f) with overlays of the simulated ABF-STEM structures.

Marten further showed the stability of the (111) interface in agreement with the calculations by Zhang. Up to this point all calculations were performed for a temperature of 0 K, while Ivashchenko [22] included thermal effects, using quantum molecular dynamic calculations (QMD), onto monolayer interfaces on the (001) and (111) planes with both 1:1 and 3:4 stoichiometry and B1 coordination. These calculations showed a stable (111) interface even up to 1400 K, while the (001) interface restructured into an overcoordinated, amorphous like, structure at 300 K. At 1400 K the same interface assumed a structure where Si atoms were either octahedrally (B1) or tetrahedrally (B3) coordinated. However, forming Si vacancies in the B1 structure for both interfaces was shown to be energetically favored, where the $Si_{0.75}N$ and Si_3N_4 were found to be most favorable for (001) and (111) interfaces, respectively. In summary, despite extensive efforts, predominantly through theoretical approaches, the actual structure of the SiN_x embedded between TiN layers remains an open and unsolved question.

Here, we investigate the crystal structure and occupancy of cubic SiN_x embedded in a single crystal TiN/SiN_x multilayer. The investigation is performed though corroborating aberration corrected scanning transmission electron microscopy ((S)TEM) and electron energy loss spectroscopy (EELS) supported by image simulations and theoretical calculations.

II. RESULTS AND DISCUSSION

The microstructure of the multilayer was investigated by means of (S)TEM and the results are shown in Fig. 1. The complete multilayer structure as observed by high angle annular dark field STEM (HAADF-(S)TEM) is shown at the top half of the image in Fig. 1(a), including the TiN seed below and the MgO substrate at the bottom. The multilayer exhibits diffraction contrast features that extend through all the layers, which indicates that the entire multilayer structure is grown epitaxially as a single crystal.

In the bottom half of Fig. 1(b), a magnified view from the indicated area in Fig. 1(a) shows the first few SiN_x layers. The first SiN_x layer (dark) exhibits a stronger appearance than the subsequent SiN_x layers. The origin of this difference is related to the high quality seed, which was grown at a higher temperature than the following layers. Hence, the initial TiN/SiN_x interface assumes a sharper and better defined appearance in comparison to the successive interfaces. The following interfaces are introduced at lower temperatures, resulting in surface roughness, which partly accumulates through the structure. Accordingly, the initial TiN/SiN_x interface is the sharpest and exhibits the clearest projection of the SiN_x structure. Consequently, this layer is investigated in detail below.

Figures 1(c)–1(f) show the initial SiN_x layer and the embedding TiN layers with atomic resolution conditions at HAADF-(S)TEM dark field conditions [Figs. 1(c) and 1(d)] and at annular bright field STEM (ABF-(S)TEM) bright field conditions [Figs. 1(e) and 1(f)]. In Figs. 1(c) and 1(e) the structure is oriented along ⟨100⟩,while the sample has been rotated by 45° to ⟨110⟩ in Figs. 1(d) and 1(e). HAADF and ABF images from the same orientation were acquired in parallel, while all images were obtained from the same location on the sample. While the HAADF-(S)TEM images are sensitive to atoms with high atomic mass ($I \sim Z^2$), the images acquired by ABF-(S)TEM, which is a semicoherent method, are aimed at optimizing contrast from light elements (such as N) [23]. As ABF-(S)TEM is a bright field method, the atoms are presented as dark, while they are bright for HAADF-(S)TEM. A section of the SiN_x layer from each ABF image is further magnified, false colored for improved contrast below, and shown in Figs. 1(g) and 1(h). ABF-(S)TEM image simulations representing 20-nm-thick slabs of NaCl (B1) coordinated cubic SiN_x, with the Si and N positions indicated are overlaid in the colored images.

The structure is continuous through the TiN/SiN_x layers. Though the interface is difficult to precisely identify by ABF-(S)TEM, the HAADF-(S)TEM images reveal an undulating SiN_x/TiN interface which locally changes the thickness of the SiN_x layer.

As can be seen in the ⟨100⟩ orientation in Figs. 1(c) and 1(e), the structure in both images and simulations assume a cubic symmetry (some sample drift is observed in the (S)TEM images). In this projection of the B1 structure, Si and N atoms are aligned on top of each other. In contrast, the zincblende (B3) structure would also exhibit a cubic appearance, but with the Si sublattice separated from the N sublattice in this projection (see the Supplemental Material for simulated structures [24]). For the ⟨110⟩ orientation in Figs. 1(d) and 1(f)], the structure assumes an entirely different appearance. As can be seen from the simulation of the B1 structure, the projected atomic columns are laterally aligned in rows with distinctly different contrast. These contrast differences arise because the projected columns exclusively contain either Si or N. The simulated B1 structure image corresponds well to the experimental image, which is distinctly different from the B3 simulation. In the B3 structure, Si and N are grouped in pairs, aligned along the ⟨001⟩ direction orientation (see the Supplemental Material for simulated images [24]). Consequently, the combined ABF-(S)TEM images provide evidence that the

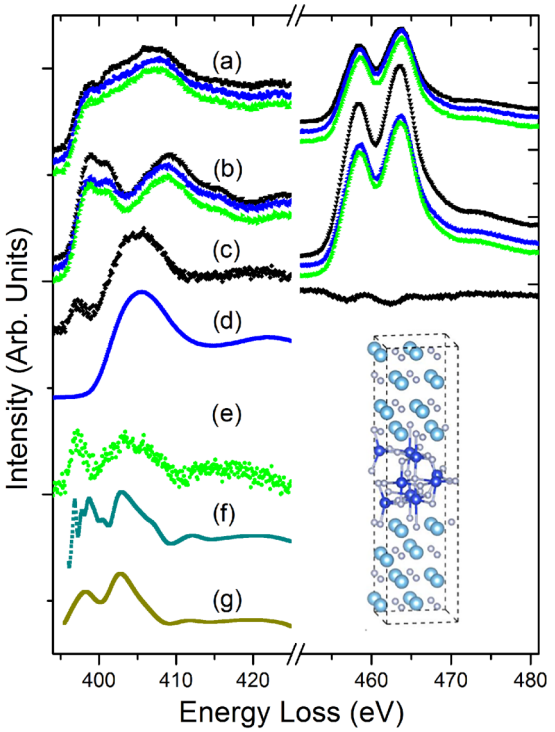

FIG. 2. ELNES fine structures of the TiN/SiN_x nanomultilayer structure revealing the N-K edge and Ti-$L_{3,2}$ edges. The top spectra in (a) stem from the first three SiN_x layers in the multilayer structure. The second line of spectra in (b) originate from the TiN seed and following two TiN layers. In the middle, (c), the extracted SiN_x spectrum (SiN_x/TiN) is shown with an amorphous SiN_x reference spectrum in (d). (e) is the extracted N-K edge associated with crystalline SiN_x is shown. The following two spectra originate from a TELNES3 calculation in its pristine state (f) and broadened (2 eV) in (g). The associated supercell on which the calculations were performed, is shown to the right.

epitaxially stabilized cubic SiN_x assumes a B1 based crystal structure, by pseudomorphing the embedding TiN.

To further evaluate the SiN_x structure and to address the stoichiometry, electron energy loss spectra were recorded from the multilayer. The core-loss EELS spectra are shown in Fig. 2, revealing the N-K (left) and the Ti-$L_{3,2}$ (right) electron energy loss near edge structures (ELNES). The spectra are extracted from a spectrum image (SI), recorded across a region similar to the bottom figure in Fig. 1(a) and through averaging of the signal in the first three layers of each compound. The spectra in Fig. 2 are normalized with respect to the integrated N-K edge. Due to a variety of experimental constraints such as the limited thickness, probe shape, averaging across layers, and delocalization of the core-loss information from adjacent TiN layers, the signal from the SiN_x layers also include a contribution from TiN as can be seen by the presence of a Ti-$L_{3,2}$ component in the three SiN_x spectra (a) in Fig. 2. The corresponding situation is seen to a reduced extent for the three TiN spectra (b), which includes a reference TiN spectrum from the seed (black). Since for the first two TiN layers, the TiN signal is delocalized into the SiN_x layers, and vice versa, the Ti-$L_{3,2}$ intensity of the TiN layers is lower than in the seed. Additionally, the TiN N-K edge fine structure appears slightly different between the TiN seed and the multilayer TiN layers, indicating an influence from nearby layers. The seed signal, corresponds well with previous measurements and calculations [25,26]. The differences observed in the N-K TiN layer signals suggest an electronic exchange with the embedded SiN_x layers. In order to extract the pure N-K SiN_x fine structure and separating the delocalized TiN information from the SiN_x, the spectrum from the first SiN_x layer was normalized using the Ti-$L_{3,2}$ edge against the TiN seed spectrum and subsequently subtracting the TiN seed information. The result of this procedure and the pure N-K SiN_x fine structure is shown in (c). As can be seen from the simultaneously reduced Ti-$L_{3,2}$ edge in (c), residual undulations of the delocalized TiN signal remain in the pure SiN_x spectrum. These undulations suggest that the Ti-$L_{3,2}$ edge is subject to a slight chemical shift in the vicinity of the SiN_x as compared to the TiN seed, supposedly through a local shift in the Fermi level. The corresponding subtraction of nearby TiN layers from the first SiN layer yields similar results, but signal-to-noise is better for the TiN seed signal and consequently reduces noise in the TiN subtracted SiN_x spectrum.

The extracted N-K SiN_x signal has a distinct shape with a small peak roughly at 1–2 eV from the edge onset followed by a more intense and broad peak centered ~10 eV from the edge onset. The latter peak is indicative of amorphous SiN_x, and pockets of amorphous SiN_x are observed throughout the SiN_x layers (as can be seen in Fig. 1), although the multilayer itself remains epitaxial. Note that the thickness of the present SiN_x layers is the maximum attainable prior to collapsing the epitaxial properties. Additionally, the high current electron beam is observed to amorphize the SiN_x layers during extended analysis. Hence, the subtracted signal in (c) is the combination of crystalline SiN_x and amorphous SiN_x. To subtract the amorphous SiN_x and to arrive at a final fine structure of the crystalline SiN_x, a high quality amorphous SiN_x signal was recorded (d) and consequently subtracted with the result shown in (e). This final spectrum exhibits a prepeak at 1–2 eV after edge onset and an asymmetric broader peak centered at ~8 eV after edge onset.

For fine structure comparison, the corresponding TELNES3 calculated N-K SiN_x spectrum was obtained from different supercells. For simplicity, only the spectrum from a B1- based "Si_3N_4" layer is shown at the bottom of Fig. 2 in unbroadened (f) and broadened (g) form together with the corresponding supercell. (See the Supplemental Material for additional spectra and supercells [24]). The "Si_3N_4" supercell exhibits vacancies on the Si site in the SiN_x layer, as this has been shown to be energetically favorable [16,17]. The spectrum was obtained in a way that follows the same procedure of extracting the experimental SiN_x signal, i.e., by subtracting the spectra of pure bulk TiN. (See the Supplemental Material for a description of this procedure [24]).

The calculated spectrum displays a complex variation of small and narrow prepeaks in the initial spectrum. However, the spectrum also reveals an asymmetric broad peak, which drops to a local intensity minima at ~12 eV after the spectrum onset. From calculations on other supercells, the position of this broad peak shifts to higher energy losses with decreasing number of Si atoms in the supercell, followed by an increasing

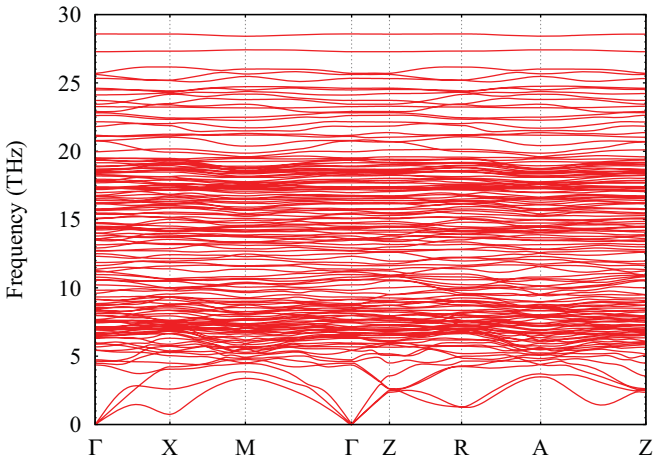

FIG. 3. Phonon spectra of the TiN-Si_3N_4 ML system.

number of initial peaks. Consequently, the position of this peak is significant since it identifies a shift in the Fermi level for the considered systems. This can be understood from N as being the most electronegative element and Si being more electronegative than Ti. With this elemental configuration, fewer electrons are available for N in thin SiN layers over the thick layers. Upon the introduction of Si vacancies in the SiN_x layer even less electrons are available for N, which substantially shifts the Fermi level and introduces a redshift to the second peak, and serves as an indicator of the Si:N stoichiometry.

While comparing the calculated vacancy dependent broadened spectrum for Si_3N_4 and the experimental in Fig. 3, a qualitative match is found. For the other considered supercells, the second peak is positioned too close to the edge onset. These results indicate that the SiN_x hosts vacancies on the Si site.

Concerning the matching spectra of the B1 based Si_3N_4 structure with the EELS experiment, the stability of this structure has not been investigated by theoretical means. First and foremost, Si_3N_4 is known to be the most stable system [16,17]. Although the Si vacancies can be configured in a variety of coordinations, only one of these is presently considered in order to arrive at a qualitative comparison to the experimental one and for a stability investigation. The number of extensive calculations to arrive at the most energetically favorable vacancy coordination is beyond the scope of this contribution, because that requires extensive variations in layer thickness, flatness, and vacancy distribution.

From a dynamic stability point of view, bulk B1-SiN was shown to be unstable [19], although it should be considered that B1-SiN could be stabilized through pseudomorphic forces in thin layers (thicker layers assume an amorphous state at experimental conditions). For the dynamical stability investigation of the epitaxially stabilized SiN_x the phonon dispersion relations of the TiN/B1-Si_3N_4 heterostructure were calculated by considering a 3 ML Si_3N_4/3 ML TiN system (see the Supplemental Material for further details [24]). Note that an increase of the thickness of TiN, which is dynamically stable in the bulk must further stabilize the system [21]. The result is shown in Fig. 3 and as can be seen, all the frequencies are real. Therefore, the presently investigated heterostructure is dynamically stable. Moreover, in contrast to the bulk B1 SiN, where instability connected with optical vibrations is seen as an imaginary frequency almost in the whole Brillouin zone [20], the TiN-Si_3N_4 ML system has the hard optical part of the spectra. Comparing our results to vacancy-free TiN-SiN with the B3 crystal structure of SiN [22], we see that the hard optical parts for both systems are similar. However, in our case we observe two high-frequency local phonons at 27 and 28 THz corresponding to vibrations of atoms near the vacancy.

Consequently, the B1-Si_3N_4 structure was found to be dynamically stable from a theoretical perspective as investigated, which corroborates the experimental findings by ABF-STEM and EELS.

III. CONCLUSIONS

The crystal structure of metastable cubic SiN_x embedded between TiN(001) templates was addressed. The structure was experimentally investigated by ABF- and HAADF-(S)TEM along with fine structure ELNES spectroscopy. The acquired experimental data was compared with STEM image simulations and fine structure calculations subject to experimentally relevant conditions. The ABF-(S)TEM imaging results decidedly show that the metastable SiN_x assumes the structure of the adjacent TiN, i.e., a NaCl (B1) structure, and grows seamlessly between the TiN layers. It is inferred that pseudomorphic forces act to stabilize the SiN_x layers. Additionally, the spectroscopic investigation corroborates the (S)TEM findings and additionally indicates that the SiN_x layer hosts Si vacancies. The results present a key towards an advanced understanding of the interface structure in transition metal nitride/SiN_x nanocomposites for ultrahard coatings.

The datasets generated during and/or analyzed during the current study are available from the corresponding author upon reasonable request.

ACKNOWLEDGMENTS

The Swedish Research Council (VR) is acknowledged for funding through the project Grants No. 2008–405, No. 2012–4359, No. 2015–04391, and No. 2016–04412 as well as the Swedish Foundation for Strategic Research (SSF) through FunCase and the Research Infrastructure Fellow program No. RIF 14–0074, as well as SRL Grant No. 10–0026. The Knut and Alice Wallenberg Foundation is acknowledged by L.H. and P.O.Å.P. for support of the electron microscopy laboratory in Linköping and by W.O. and I. A. A. for the project Strong Field Physics and New States of Matter 2014–2019 (CoTXS). P.O.Å.P. further acknowledges the M. Bergwall foundation for funding. L.H., P.O.Å.P., I.A.A., and W.O. acknowledge support from the Swedish Government Strategic Research Area in Materials Science on Functional Materials at Linköping University (Faculty Grant SFO-Mat-LiU No. 2009 00971). Theoretical analysis of vibrational properties was supported by the Ministry of Education and Science of the Russian Federation (Grant No. 14.Y26.31.0005). Calculations of the electronic structure were supported by the Ministry of Education and Science of the Russian Federation

in the framework of Increase Competitiveness Program of NUST "MISIS" (No. K2-2017-080) implemented by a governmental decree dated 16 March 2013, No. 211. The simulations were carried out using supercomputer resources provided by the Swedish National Infrastructure for Computing (SNIC) performed at the National Supercomputer Centre (NSC).

P.O.Å.P. conceived the study and performed the microscopy with input from J.P. A.F. performed the image simulations and prepared the manuscript with input from the other authors. W.O., B.A., and M.B. performed the theoretical calculations and outlined them together with I.A.A. and P.O.Å.P. All authors analyzed and discussed the data.

The authors declare no competing financial interests.

[1] E. O. Hall, Proc. Phys. Soc. London B **64**, 747 (1951).
[2] N. J. Petch, J. Iron Steel Inst. **174**, 25 (1953).
[3] S. Veprek, J. Vac. Sci. Tech. A **17**, 2401 (1999).
[4] J. Schiøtz, F. D. Di Tolla, and K. W. Jacobsen, Nature **391**, 561 (1998).
[5] L. Hultman, J. Bareño, A. Flink, H. Söderberg, K. Larsson, V. Petrova, M. Odén, J. E. Greene, and I. Petrov, Phys. Rev. B **75**, 155437 (2007).
[6] S. Veprek, High Press. Res. **26**, 119 (2006).
[7] C. Iwamoto and S.-I. Tanaka, J. Am. Ceram. Soc. **81**, 363 (1998).
[8] J. S. Koehler, Phys. Rev. B **2**, 547 (1970).
[9] J. Xu, M. Gu, and G. Li, J. Mater. Sci. **35**, 3535 (2000).
[10] H. Söderberg, M. Odén, J. M. Molina-Aldareguia, and L. Hultman, J. Appl. Phys. **97**, 114327 (2005).
[11] H. Söderberg, M. Odén, A. Flink, J. Brich, P. O. Å. Persson, M. Beckers, and L. Hultman, J. Mater. Res. **22**, 3255 (2007).
[12] M. Kong, W. Zhao, L. Wei, and G. Li, J. Phys. D **40**, 2858 (2007).
[13] X. Hu, H. Zhang, J. Dai, G. Li, and M. Gu, J. Vac. Sci. Technol. A **23**, 114 (2005).
[14] R. F. Zhang, A. S. Argon, and S. Veprek, Phys. Rev. Lett. **102**, 015503 (2009).
[15] R. F. Zhang, A. S. Argon, and S. Veprek, Phys. Rev. B **79**, 245426 (2009).
[16] S. Hao, B. Delley, S. Veprek, and C. Stampfl, Phys. Rev. Lett. **97**, 086102 (2006).
[17] S. Hao, B. Delley, and C. Stampfl, Phys. Rev. B **74**, 035402 (2006).
[18] S. Hao, B. Delley, and C. Stampfl, Phys. Rev. B **74**, 035424 (2006).
[19] B. Alling, E. I. Isaev, A. Flink, L. Hultman, and I. A. Abrikosov, Phys. Rev. B **78**, 132103 (2008).
[20] T. Marten, E. I. Isaev, B. Alling, L. Hultman, and I. A. Abrikosov, Phys. Rev. B **81**, 212102 (2010).
[21] T. Marten, B. Alling, E. I. Isaev, H. Lind, F. Tasnádi, L. Hultman, and I. A. Abrikosov, Phys. Rev. B **85**, 104106 (2012).
[22] V. I. Ivashchenko, S. Veprek, P. E. A. Turchi, and V. I. Shevchenko, Phys. Rev. B **85**, 195403 (2012).
[23] S. D. Findlay, N. Shibata, H. Sawada, E. Okunishi, Y. Kondo, and Y. Ikuhara, Ultramicroscopy **110**, 903 (2010).
[24] See Supplemental Material at http://link.aps.org/supplemental/10.1103/PhysRevMaterials.2.093608 for experimental methods and details on calculations of the phonon spectra, the EELS spectra, and image simulations.
[25] D. Holec, R. Rachbauer, D. Kiener, P. D. Cherns, P. M. F. J. Costa, C. McAleese, P. H. Mayrhofer, and C. J. Humphreys, Phys. Rev. B **83**, 165122 (2011).
[26] A. Flink, R. M'Saoubi, F. Giuliani, J. Sjölén, T. Larsson, P. O. Å. Persson, M. P. Johansson, and L. Hultman, Wear **266**, 1237 (2009).